Multiple Influences of Molybdenum on the Precipitation Process in a Martensitic PH Stainless Steel

metals

MDPI

Article

Multiple Influences of Molybdenum on the Precipitation Process in a Martensitic PH Stainless Steel

Mattias Thuvander [1,*], Marcus Andersson [1,2] and Krystyna Stiller [1]

[1] Department of Physics, Chalmers University of Technology, SE-41296 Göteborg, Sweden; marcus.c.andersson@skf.com (M.A.); stiller@chalmers.se (K.S.)
[2] Research and Technology Development, SKF Group, SE-41550 Göteborg, Sweden
* Correspondence: mattias.thuvander@chalmers.se; Tel.: +46-31-772-3322

Received: 22 September 2019; Accepted: 17 October 2019; Published: 19 October 2019

Abstract: Molybdenum has been found to influence the complex precipitation process in a martensitic precipitation hardening stainless steel during aging at 475 °C in several different ways. Three steels with different Mo content (0, 1.2 and 2.3 at.%) were investigated. Studies of the microstructure were performed with atom probe tomography and energy filtered transmission electron microscopy. It is shown that, at the initial stage of aging, a faster nucleation of Cu-rich clusters takes place with increasing Mo content. The Cu-clusters act as precipitation sites for other solute elements and promote the nucleation of Ni-rich phases. During further aging, a higher Mo content in the material instead slows down the growth and coarsening of the Ni-rich phases, because Mo segregates to the interface between precipitate and matrix. Additionally, Mo promotes decomposition of the matrix into α and α′ regions. After longer aging times (>40 h) quasicrystalline Mo-rich R′ phase forms (to a greater extent in the material having the highest Mo content). The observations serve to understand the hardness evolution during aging.

Keywords: atom probe tomography; energy filtered transmission electron microscopy; aging; precipitation; stainless steels

1. Introduction

Precipitation hardening (PH) is the basis for high strength and toughness in martensitic PH stainless steels (also called maraging steels) [1,2]. After solution annealing at 1050–1150 °C and cooling, the matrix becomes supersaturated with alloying elements like Ni, Ti, Al and Cu. When the material is subjected to an additional heat treatment (aging) at around 450–550 °C, intermetallic phases are precipitated in the matrix, which results in highly increased strength. As the precipitates are just a few nanometers in size and the number density is high, atom probe tomography (APT) has been an important tool in many investigations [3–8].

During the 1990s, a new martensitic PH stainless steel, named Nanoflex®, was developed by Sandvik Materials Technology (SMT). Due to a very complex precipitation process, the ultimate tensile strength of Nanoflex® reaches 3 GPa with retained high ductility [9]. The material also shows a remarkable resistance to softening during prolonged aging. To understand the unique precipitation process in Nanoflex®, extensive research has been conducted over the years [9–12]. It has been shown using APT that Cu-rich clusters nucleate within a few minutes during aging at 475 °C and that Ni, Al and Ti surrounds these Cu-rich clusters within 5 min of aging [9,13,14]. After aging for a few hours, two sets of Ni-rich precipitates, η-Ni_3(Ti, Al) and γ′-Ni_3(Ti, Al, Si), are observed [12]. The Ni-rich precipitates are in direct contact with the Cu-rich 9R precipitates, forming co-precipitates.

The η precipitates are larger than the γ′ and have a rod-like morphology, while the γ′ precipitates are approximately spherical. After 40 h, Cr-rich α′ precipitates have appeared in contact with the Ni-rich phases [12,15]. Furthermore, a phase transformation of the γ′-Ni_3(Ti, Al, Si) phase into G-$Ni_{16}Ti_6Si_7$ takes place at this stage of the aging process (between 40 and 100 h). Finally, after 100 h of aging, a Mo-rich phase with a composition corresponding to that of the quasi-crystalline R′ phase has been observed [10,12].

Precipitation and segregation at lath boundaries in Nanoflex® have likewise been studied in detail [16]. It was shown that Mo, Si and P segregate already after 5 min of aging and after 100 h a 5 nm thick Mo-rich precipitate film had formed, with a composition very similar to R′. Additionally, precipitation of 9R and elongated η was observed at the lath boundaries. These precipitates grew marginally faster than the corresponding precipitates in the matrix and the area number density was higher at the lath boundary. Interestingly, γ′, G and α′ precipitates were not observed at the lath boundaries.

In earlier investigations the exceptionally high strength resulting after a few hours of aging (for commercial applications the aging time is typically 1–4 h) was attributed to precipitation of R′ and the unique properties of such quasicrystals [10]. However, it was later shown that R′ is not present unless the aging is extended to more than 40 h [12], and it was proposed that R′ rather contributes to the resistance against over-aging than the peak-strength. It is clear that Mo plays an important role for the aging response of Nanoflex® and it has previously been compared with the Mo-free steel Carpenter 455® [9,14]. Despite the similarity in composition, the aging response of the two steels differs significantly. While the hardness of Nanoflex® continues to increase during prolonged aging at 475 °C, Carpenter 455® softens already after a few hours. The influence of Mo on the precipitation process has also been considered in earlier investigations [13,14]. These comparisons were, however, not conclusive, due to differences in deformation degree and Al content of the materials compared. In order to fully understand the influence of Mo on the precipitation process during aging, test alloys have now been investigated. Their composition and deformation are similar, but the Mo content varies.

2. Materials and Methods

Three different alloys, produced by SMT, with different Mo contents (see Table 1) have been studied in this work. Although the variation in Mo is the main difference between the alloys, it should be noted that there are also other differences, e.g., in the Si and Al contents. The alloys with Mo concentrations 0.01 at.%, 1.2 at.% and 2.3 at.% are designated 0Mo, 1Mo and 2Mo respectively, in this paper. The material 2Mo is identical to commercial Nanoflex®. The materials were solution treated at 1050 °C for three minutes and then quenched in water. In order to maximize the fraction of martensite, the materials were deformed by rolling into strips, resulting in a deformation degree of 83% for all three alloys. The materials were then aged at 475 °C for up to 100 h.

Table 1. Composition of the investigated materials (at.%), with Fe as balance.

Material	Cr	Ni	Mo	Cu	Ti	Al	Mn	Si	C
0Mo	12.8	8.3	0.01	1.74	1.25	0.90	0.40	0.43	0.02
1Mo	13.0	8.4	1.18	1.75	1.11	0.85	0.40	0.38	0.02
2Mo	13.0	8.5	2.31	1.68	1.10	0.69	0.30	0.23	0.03

APT was carried out using two local electrode atom probe versions; LEAP 3000X Si and LEAP 3000X HR (both from Imago Scientific Instruments, Madison, WI, USA) [17]. The HR type is equipped with a reflectron lens for improved mass resolution, whereas the Si version has higher detection efficiency, about 57% compared to 37% for the HR. All APT analyses were performed using a pulse fraction of 20% of the DC voltage at a specimen temperature of 70 K. Needle-shaped specimens were prepared by a two-step electropolishing procedure where in the first step the specimen was electropolished in an electrolyte layer (10% perchloric acid in 20% glycerol and 70% methanol) floating

atop Galden® until a suitable neck was formed and in the second step the entire specimen was electropolished in a weak electrolyte (2% perchloric acid in 2-butoxyethanol). For evaluation of the early stages of clustering, the radial distribution function (RDF), which is closely related to the pair correlation described in Reference [18], was used. In these calculations, the incremental radius step was 0.1 nm.

Materials aged for 100 h were investigated with energy filtered transmission electron microscopy (EFTEM) on a Philips CM 200 FEG-TEM, equipped with a Gatan Image Filter. The jump-ratio images were produced using the Fe-$M_{2\text{-}3}$, Cr-$L_{2\text{-}3}$ and Mo-$M_{4\text{-}5}$ edges in the energy-loss electron spectrum [19,20]. Thin TEM/EFTEM foils were prepared using the following steps; tripod polishing, electrochemical polishing and low angle ion-beam milling.

3. Results

3.1. Hardness

The hardness, and the hardness increase relative to the respective solution annealed material, of the three alloys as a function of aging time at 475 °C is presented in Figure 1. In solution annealed materials the hardness increases with Mo content. In the aged conditions, it is clear that the initial response becomes faster with increased Mo content, with an increase of 170 HV after 5 min. In 2Mo, compared to an increase of 120 HV for the other two materials. On the other hand, softening sets in after shorter times when the Mo content decreases. For the times investigated (5 min, 1 h, 4 h, 40 h and 100 h), 0Mo, 1Mo and 2Mo have their highest hardness after 4 h, 40 h and 100 h, respectively. It is also interesting to note that the maximum hardness increase is about 240 HV for all three materials.

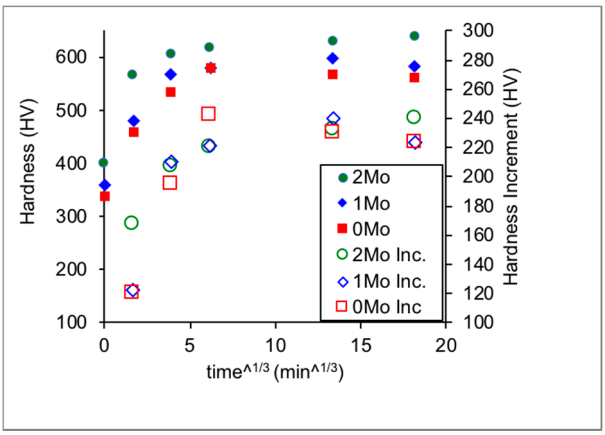

Figure 1. Hardness and incremental hardness during aging at 475 °C. The times included are 5 min., 1 h, 4 h, 40 h and 100 h.

3.2. Atom Probe Tomography

3.2.1. Unaged Materials and Materials Aged for 5 min at 475 °C

In unaged materials, a homogeneous distribution of all alloying elements was observed, both directly in atom maps and in RDF plots. After 5 min of aging, visual inspection showed clear signs of clustering of Cu, Al, Ti and Ni in all three alloys, with an increased degree of clustering with increased Mo content. This is confirmed by bulk normalized RDF curves of Cu-Cu, Ti-Ti and Cu-Ti presented in Figure 2. Here, the first element refers to the center atom, and the second to the element for which the concentration is measured. In these diagrams, values significantly larger than unity for short distances indicate clustering (co-clustering in the case of Cu-Ti). It is clear that the degree of clustering increases with increasing Mo content for the three pairs presented, both regarding concentration and size. For Cu-X the same trend was observed in all three alloys with X = Al, Ti, Ni, Mn and Si, in order

of decreasing clustering tendency. Clustering of Mo or Cr was not observed in any of the alloys after aging for 5 min. (RDF curves of Mo-Mo, Cr-Cr, Cu-Mo and Cu-Cr show no increase in concentration for short distances).

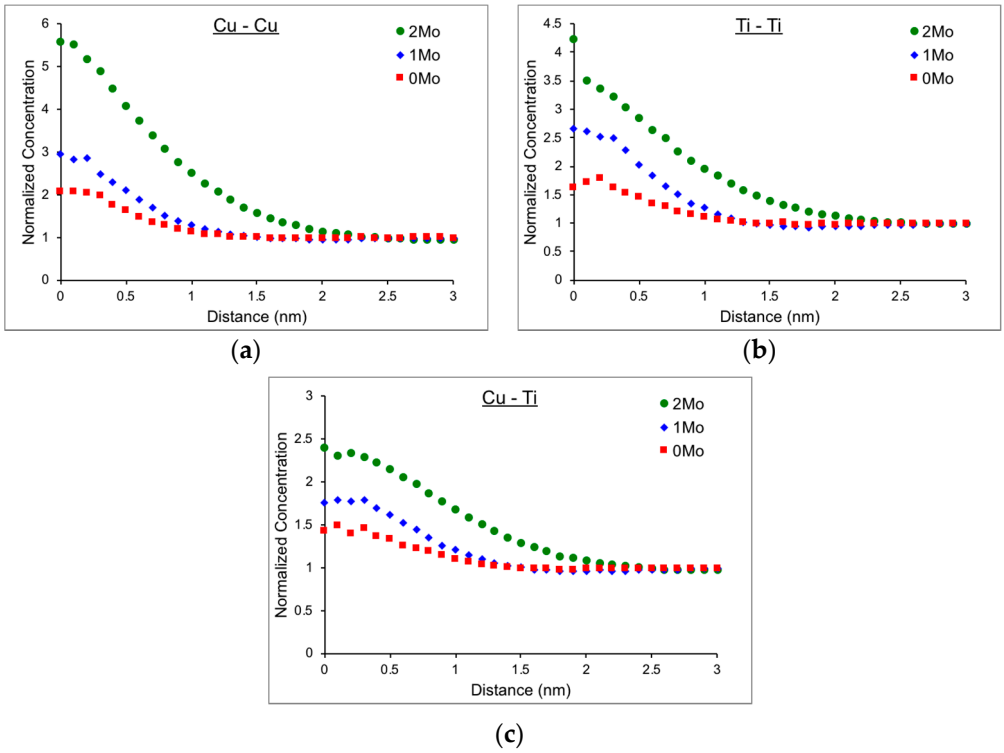

Figure 2. Normalized radial distribution function (RDF)-curves from atom probe tomography (APT) analysis after aging at 475 °C for 5 min: (**a**) Cu-Cu; (**b**) Ti-Ti; (**c**) Cu-Ti. The first element refers to the center atom and the second to the element for which the RDF is shown.

3.2.2. Materials Aged for 4 h at 475 °C

Three types of precipitates, one Cu-rich type and two Ni-rich types, were found after 4 h of aging. The existence of two sets of Ni-rich precipitates, in direct contact with Cu-rich precipitates, was observed in all three materials, see Figure 3. This agrees with previous observations in Nanoflex® (2Mo) [12]. The average diameter of the Cu-rich particles was about 2 nm. The composition of the Ni-rich precipitates, for all three materials, is presented in Table 2. The vast majority of the Ni-rich precipitates had an approximately spherical morphology and the particles were enriched in Ti, Al and Si, while some somewhat larger precipitates were elongated and had a composition close to Ni_3(Ti, Al), with a very low concentration of Si. These precipitates are presumably γ′-Ni_3(Ti, Al, Si) and η-Ni_3(Ti, Al), respectively [12]. The Si-containing γ′-particles, in all three materials, contained 5 at.% or more of Si after 4 h of aging. To calculate the composition of the two Ni-rich phases, isosurfaces of 2 at.% Si were used for the γ′-precipitates and isosurfaces of 30 at.% Ni were used for the η-Ni_3(Ti, Al) precipitates (not including the γ′-precipitates). A clear dependence between the precipitate chemistry and the Mo content of the steel was observed. In the 1% Mo material (1Mo), the γ′-precipitates had the lowest Ni and Ti content and the highest Fe content, see Table 2, indicating that these precipitates were the least developed for the mid Mo content. On the other hand, both types of precipitates in the Mo-free (0Mo) material were richest in Ni and Ti and poorest in Fe. Moreover, Table 2 reveals that the Si content of the γ′-precipitates increases slightly as the Mo content decreases.

The morphology of the η-Ni_3(Ti, Al) precipitates changed during the aging treatment from slightly elongated to cigar-shaped. After aging for 4 h the η-Ni_3(Ti, Al) type was larger in 0Mo (up to 5 nm)

than in 1Mo and 2Mo. The average diameter of the γ′-precipitates was established to 4 nm for 0Mo, 2 nm for 1Mo and 3 nm for 2Mo.

At this stage of the aging, weak segregation of Cr and Mo to the interface between Ni-rich precipitates and the matrix was observed in 2Mo [12], but not in 1Mo or 0Mo.

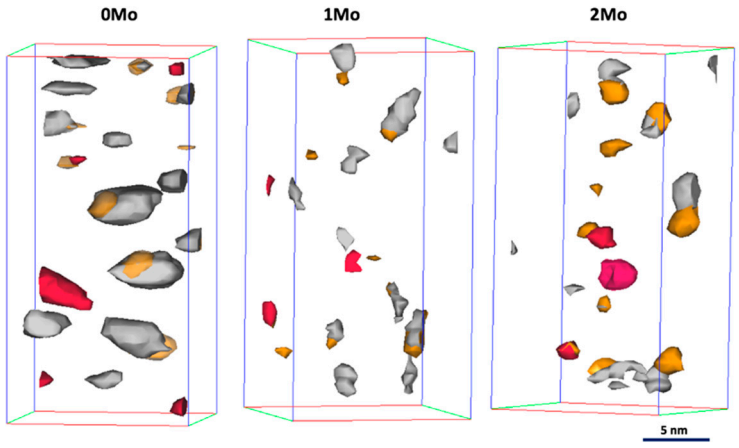

Figure 3. APT reconstructions after aging at 475 °C for 4 h. Cu-rich precipitates are shown in orange, Ni-rich precipitates containing more than 5 at.% Si (γ′-Ni_3(Ti, Al, Si)) in red and less than 5 at.% Si (η-Ni_3(Ti, Al)) in grey.

Table 2. Composition of the two types of Ni-rich precipitates after aging for 4 h at 475 °C (at.%).

Material	γ′-Ni_3(Ti, Al, Si)					η-Ni_3(Ti, Al)			
	Ni	Ti	Al	Si	Fe	Ni	Al	Ti	Fe
0Mo	44.2 ± 1.9	14.9 ± 1.4	7.4 ± 1.0	7.8 ± 1.0	16.7 ± 1.5	65.5 ± 1.8	6.4 ± 0.9	20.9 ± 1.5	2.8 ± 0.6
1Mo	32.0 ± 0.8	9.9 ± 0.5	5.4 ± 0.4	7.2 ± 0.5	34.5 ± 1.2	61.7 ± 1.7	6.4 ± 0.9	15.5 ± 1.2	10.5 ± 1.1
2Mo	37.4 ± 0.9	11.6 ± 0.6	5.8 ± 0.5	6.1 ± 0.5	28.5 ± 0.9	56.7 ± 1.5	6.0 ± 0.7	16.1 ± 1.1	13.6 ± 1.1

3.2.3. Materials Aged for 40 h at 475 °C

Further development of the precipitates was observed after 40 h of aging, see Figure 4 and Table 3. In 0Mo, the Cu-rich precipitates became larger, reaching about 6 nm diameter on average. Furthermore, a clear rejection of Al from the Si-containing Ni-rich precipitates was observed in 0Mo, see proxigram in Figure 5. The precipitates became instead rich in Si and their composition was similar to $Ni_{16}Ti_6Si_7$, i.e., the G-phase. The same development, but slightly less pronounced, was also observed in 1Mo. In 2Mo, the changes compared to the 4 h aging were much smaller, and probably the Si-containing precipitates were still the γ′-phase. The average diameter of the Si-containing precipitates was 7 nm in 0Mo, 5 nm 1Mo and 4 nm in 2Mo.

The composition of the η-Ni_3(Ti, Al) phase was similar in all three materials after 40 h of aging, see Table 3, and the measured Fe content has further decreased. The size of the η-Ni_3(Ti, Al) precipitates was slightly larger when the Mo-content was lower, see Figure 4.

After 40 h of aging, Cr-rich precipitates, in contact with Ni-rich precipitates were observed in 2Mo [12], and to some extent in 1Mo, but not in 0Mo. In both Mo-containing grades, Mo enrichments were found close to the η-Ni_3(Ti, Al) precipitates, more so in 2Mo, as shown in Reference [12].

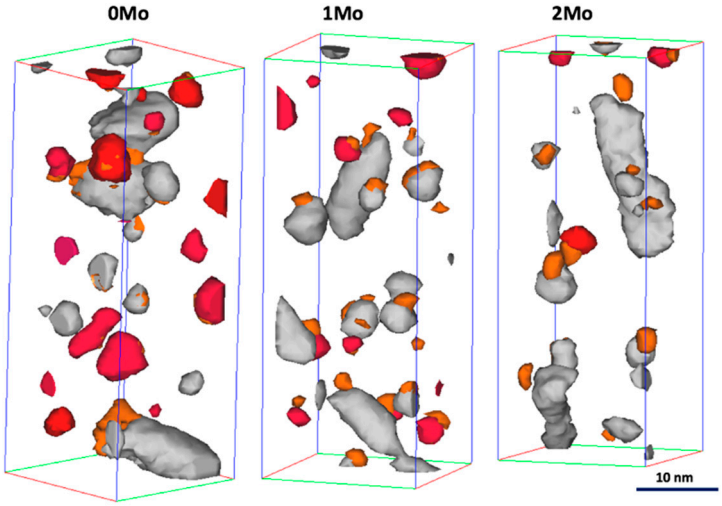

Figure 4. APT reconstructions after aging at 475 °C for 40 h. Cu-rich precipitates are shown in orange, Ni-rich precipitates containing more than 5 at.% Si (γ′ or G) in red and less than 5 at.% Si (η) in grey.

Table 3. Composition of the two types of Ni-rich precipitates after aging for 40 h at 475 °C (at.%).

Material	γ′-Ni_3(Ti, Al, Si)/G-$Ni_{16}Ti_6Si_7$					η-Ni_3(Ti, Al)			
	Ni	Ti	Al	Si	Fe	Ni	Al	Ti	Fe
0Mo	49.7 ± 1.8	15.2 ± 1.3	4.4 ± 0.7	16.3 ± 1.3	10.3 ± 1.1	69.9 ± 0.5	8.8 ± 0.3	19.2 ± 0.5	0.8 ± 0.1
1Mo	47.8 ± 2.5	14.0 ± 1.8	4.5 ± 1.1	14.3 ± 1.8	14.2 ± 1.8	67.0 ± 1.5	7.7 ± 0.9	19.7 ± 1.3	2.8 ± 0.5
2Mo	41.1 ± 2.0	13.6 ± 1.4	6.4 ± 1.0	9.2 ± 1.2	22.3 ± 1.7	68.9 ± 1.3	8.4 ± 0.8	14.9 ± 1.0	3.7 ± 0.5

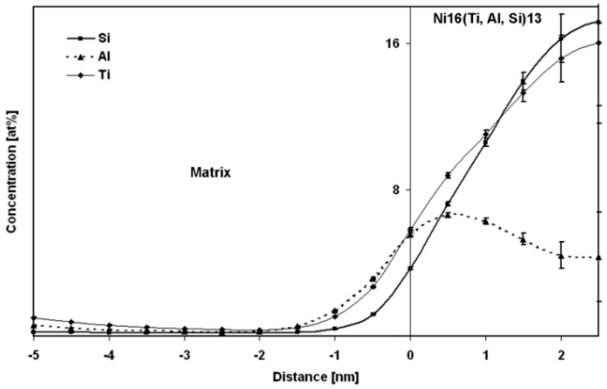

Figure 5. Proxigram obtained from Si-containing Ni-rich precipitates (G-phase) in 0Mo aged for 40 h at 475 °C showing rejection of Al.

3.2.4. Materials Aged for 100 h at 475 °C

The composition of the Ni-rich precipitates after aging for 100 h at 475 °C is shown in Table 4, and APT reconstructions showing Ni-rich and Cu-rich precipitates are shown in Figure 6. In 2Mo, the composition of the Si-containing precipitates has changed compared to after 40 h; Ni, Ti and Si have increased, whereas Al and Fe have decreased. This is interpreted as a transformation of the γ′-precipitates to G-phase [12]. For 0Mo, on the other hand, Ni and Ti have decreased significantly (Si and Al marginally) and Fe has increased. The Si-containing precipitates in 0Mo have also become smaller, which, together with the change in composition, suggests that the G-phase is not stable and is being dissolved. For 1Mo the situation is in between 0Mo and 2Mo, the Si content has increased, but Ni and Ti has decreased.

The η-Ni_3(Ti, Al) precipitates are now so large that the size cannot easily be determined using APT. From Figure 6, though, it is clear that they are largest in 0Mo. The Cu-rich precipitates have also grown

in all three materials. In 2Mo, the quasicrystalline R' phase, with composition 35Fe-34Mo-13Cr-10Ni-7Si (at.%), has previously been reported from APT analysis after 100 h of aging [12]. The Cr-rich precipitates that were observed after 40 h are still present after 100 h, but with lower number density.

Table 4. Composition of the two types of Ni-rich precipitates after aging for 100 h at 475 °C (at.%).

Material	G-$Ni_{16}Ti_6Si_7$					η-Ni_3(Ti,Al)			
	Ni	Ti	Al	Si	Fe	Ni	Al	Ti	Fe
0Mo	28.1 ± 2.2	6.0 ± 1.2	3.6 ± 0.9	14.7 ± 1.7	39.8 ± 2.4	72.8 ± 2.8	4.9 ± 1.3	15.3 ± 2.3	4.5 ± 1.3
1Mo	30.4 ± 4.2	10.1 ± 2.7	3.7 ± 1.7	21.6 ± 3.8	25.6 ± 4.0	68.8 ± 2.6	5.1 ± 1.2	16.2 ± 2.1	6.8 ± 1.4
2Mo	46.8 ± 5.3	16.8 ± 4.0	3.3 ± 1.9	21.2 ± 4.4	5.3 ± 2.4	68.8 ± 1.7	7.5 ± 1.0	12.2 ± 1.2	6.4 ± 0.9

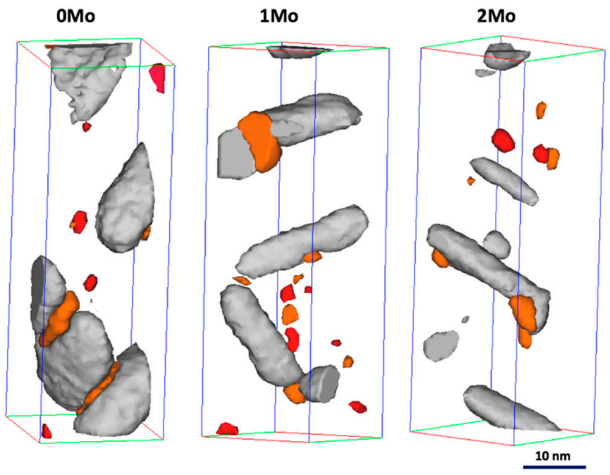

Figure 6. APT reconstructions after aging at 475 °C for 100 h. Cu-rich precipitates are shown in orange, Ni-rich precipitates containing more than 5 at.% Si (G) in red and less than 5 at.% Si (η) in grey.

3.2.5. Matrix Composition

The precipitation during aging led to a depletion of the alloying elements of the matrix. The matrix composition, i.e., the composition after removing the precipitates from the analyzed volume, after aging at 475 °C for 4 h, 40 h and 100 h is presented in Table 5. The accuracy of the measurement is not very high, as it depends on the choice of thresholds for removing the precipitates, and whether segregated regions become removed or not. Anyway, it is clear that the matrix concentration of Cu, Ti and Al are very low, already after 4 h of aging. The remaining concentration of Ni must largely be determined by the alloy Ti and Al contents. For Mo, a slow decrease is observed, which is caused by segregation to matrix/precipitates interfaces (shown in Reference [12] for 2Mo using proxigrams and atom maps), lath boundaries (shown in Reference [16] for 2Mo) and after 100 h also by the formation of R'-phase (analyzed in 2Mo using APT in Reference [12], giving the composition 35Fe-34Mo-13Cr-10Ni-7Si (at.%)).

Table 5. Composition of the matrix of the investigated materials (at.%), with Fe as balance.

Material	Cr	Ni	Mo	Cu	Ti	Al	Mn	Si
4 h of aging								
0Mo	12.2	3.2	-	0.09	0.06	0.05	0.27	0.15
1Mo	11.1	2.2	1.2	0.07	0.08	0.10	0.21	0.17
2Mo	12.9	4.2	2.1	0.08	0.05	0.04	0.14	0.08
40 h of aging								
0Mo	11.5	3.7	-	0.07	0.07	0.06	0.26	0.14
1Mo	11.4	3.0	0.9	0.07	0.06	0.04	0.23	0.09
2Mo	11.5	3.8	1.7	0.06	0.03	0.04	0.14	0.07
100 h of aging								
0Mo	12.6	3.1	-	0.06	0.03	0.05	0.23	0.26
1Mo	12.5	3.3	0.69	0.06	0.02	0.04	0.20	0.10
2Mo	11.8	4.7	1.1	0.08	0.004	0.04	0.20	0.08

3.3. Transmission Electron Microscopy

After 100 h of aging, the precipitates were large enough to be investigated with EFTEM. The Fe jump-ratio image in Figure 7 shows the aggregated distribution of Ni-rich, Cu-rich and Mo-rich phases (dark features). It is clear that the size of the cigar-shaped η-Ni_3(Ti, Al) precipitates is smaller in materials with higher Mo content, as suggested from the APT analysis, see Figure 6.

Cr jump-ratio images in Figure 7 show the distribution of Cr-rich precipitates (bright features) in all three materials. They had similar number density in 2Mo and 1Mo, while their distribution in 0Mo material was very sparse. In 2Mo, the precipitates were larger and more elongated than in 1Mo.

Jump-ratio images of Mo in 2Mo revealed the presence of Mo-rich precipitates with a diameter up to 40 nm after 100 h of aging (Figure 7). However, a large variety in both size and morphology of the precipitates was observed. The Mo content in the matrix of 2Mo was reduced to 1.1 at.%, which means that approximately 1.2 at.% had been consumed by precipitation and segregation. Regarding the Mo-poor material (1Mo), only small occasional Mo-rich precipitates were found after 100 h of aging, see arrow in Figure 7. The matrix concentration was about 0.7 at.%, meaning that 0.5 at.% of Mo had segregated/precipitates in 1Mo, i.e., less than half the amount compared to 2Mo.

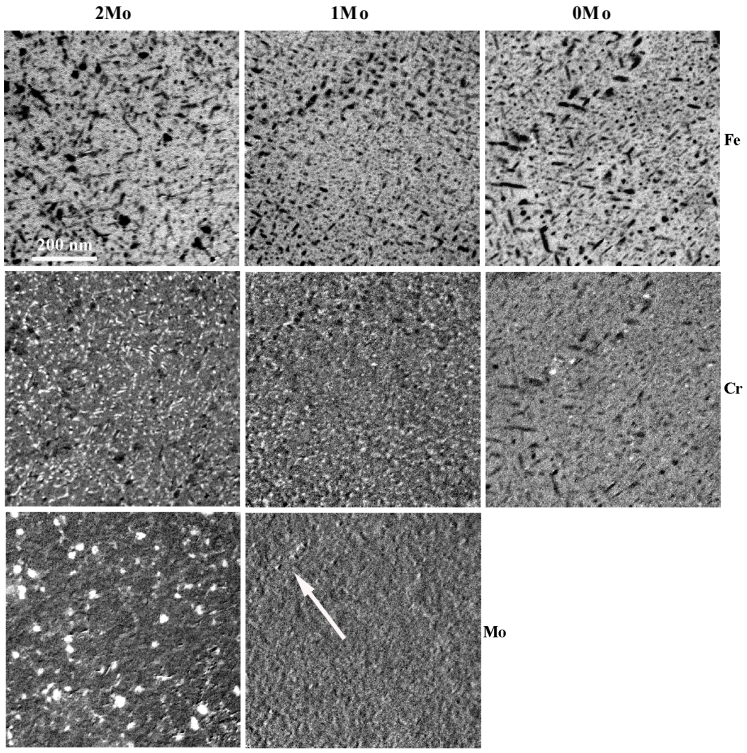

Figure 7. Energy filtered transmission electron microscopy (EFTEM) jump-ratio images of materials aged for 100 h at 475 °C, with white representing a high concentration and black a low concentration. The arrow marks a few occasional Mo-rich precipitates in 1Mo.

4. Discussion

The RDFs created from the APT data sets revealed an obvious trend of a faster clustering of Cu with increasing Mo content, see Figure 2, and thereby faster nucleation of Cu-rich precipitates and co-precipitation of Ni-rich precipitates. Thermocalc calculations also show that the solubility of Cu, in a martensitic matrix with low carbon content, decreases with increasing Mo content. This seems to explain the fast nucleation of Cu in material with a high amount of Mo. The nucleation process is further facilitated by the high deformation degree of the investigated materials that results in a high dislocation density. In the early stage of the precipitation process, here represented by the materials aged for 5 min, the nucleation of Cu in 2Mo is significantly faster than the nucleation of Ti,

see Figure 2a versus Figures 2b and 2c. The same holds for Al, Ni and Si. Thus, Cu nucleates almost immediately after the start of aging and it is clear that the Cu-rich precipitates act as nucleation sites for Ni/Ti/Al/Si-rich precipitates. This mechanism becomes less important as the Mo content decreases. The fast nucleation in 2Mo results in the highest hardness increase after 5 min of aging (see Figure 1).

As the aging treatment proceeds, two types of Ni-rich phases form, one containing Si and one not. As discussed in Reference [12], the Si-free, elongated, precipitate is most probably η-Ni_3(Ti, Al). At the early stages, the Si-containing phase is probably γ′-Ni_3(Ti, Al, Si), which later transforms to G-phase, with a much higher Si concentration. The presence of Mo influences the growth of these precipitates in two ways; it prevents their growth and it affects their composition. The influence of Mo on the growth is most clearly demonstrated in the case of the η-Ni_3(Ti, Al) phase. In the Mo-free 0Mo material, the η-Ni_3(Ti, Al) precipitates grow significantly faster between 4 and 40 h of aging than those in 2Mo and 1Mo. Moreover, these precipitates have the lowest Fe content and the highest Ni content after 4 h of aging (Table 2). The main reason for this effect is probably that Mo is rejected from the growing precipitates and is enriched at the precipitates/matrix interface [12], thereby decreasing the growth, which compensates for the slower nucleation of precipitates in the early stages of aging. An occasional deviation from the mentioned scenario is observed in the case of γ′-Ni_3(Ti, Al, Si) precipitates after 4 h of aging. The amount of Ni and Ti in these precipitates is lower in 1Mo material than in 2Mo, see Table 2. We believe that the intermediate Mo content in this material gives both relatively slow nucleation and growth of the precipitates. The combination of the two effects, results in the least developed chemistry of the γ′-Ni_3(Ti, Al, Si) precipitates at this specific aging time.

Thermocalc calculations show that the solubility limit for Cr in 2Mo is about 15 at.% at 475 °C. Precipitation of Cr-rich phase is therefore not caused by a supersaturation of Cr in the beginning of aging, but due to the modification of the matrix composition as the heat treatment proceeds. It is clear that Cr is rejected from the Cu- and Ni-rich precipitates. Thus, the same rejection mechanism, creating high local enrichment of Cr at the interface between the matrix and the Ni-precipitates, is active in all three materials. The Cr-rich precipitates are probably α′, and it is likely that Mo makes the formation faster.

The observed evolution of the precipitation makes it possible to understand the evolution of hardness. The initial hardness increase is faster with higher Mo content due to fast nucleation. On the other hand, coarsening is faster with a low Mo content due to segregation of Mo to the interfaces. With increased time the hardness continues to increase when the Mo content is high enough thanks to both a slow coarsening of the Ni-rich precipitates but also thanks to the formation of new phases, Cr-rich α′ after 40 h and Mo-rich R′-precipitates after 100 h.

Although the major difference between the three materials is the Mo content, there are also some other differences in the composition, which cannot be neglected. As seen in Table 1, the three precipitate forming elements Ti, Al and Si have the highest concentrations in 0Mo and the lowest concentrations in 2Mo. In the solution annealed state, the hardness increases with Mo content, because of the strong solid solution strengthening effect of Mo. The maximum hardness increase during aging was found to be similar (about 240 HV) in the three materials. If only considering the Mo content, it would be expected that the materials containing more Mo should display a higher hardness increase during aging, as Mo promotes the additional precipitation of α′ and R′. The reason the hardness increase is similar in the three materials is likely that the lower Mo content is balanced by higher contents of Ti, Al and Si, resulting in a somewhat larger volume fraction of Ni-rich precipitates. It is not expected that the differences in Ti, Al and Si change the type of precipitates formed, but it is likely that the relative amounts of γ′-Ni_3(Ti, Al, Si) and η-Ni_3(Ti, Al,) change, with an increase in γ′ with increased Si content. A higher Si content could also be responsible for the faster transition from γ′ to G observed in 0Mo and 1Mo compared to 2Mo.

All in all, this study has demonstrated the complex multiple influences of Mo on the evolution of precipitation during aging of the investigated type of maraging steel.

5. Conclusions

Mo affects the evolution of the microstructure of the investigated type of maraging steels in several ways:

1. Mo reduces the solubility of Cu in the martensitic matrix, which results in a faster nucleation of small Cu-rich precipitates. These precipitates promote the nucleation of Ni/Ti/Al-rich precipitates, which nucleate on the Cu-rich precipitates.
2. Mo slows down the growth and coarsening of Ni-rich phases during aging. The phase transformation of γ'-Ni_3(Ti, Al, Si) into G-$Ni_{16}Ti_6Si_7$ is also promoted by the reduction of Mo in the materials.
3. Mo promotes decomposition of the matrix into Cr-rich α' regions.
4. In the Mo-containing grades the quasicrystalline R′ phase forms after extended aging.

These effects of Mo result in a faster aging response at short times, but in an increased resistance to over-aging at longer times.

Author Contributions: Conceptualization, K.S. and M.T.; investigation, M.T. and M.A.; writing—original draft, M.A.; writing—review and editing, M.T. and K.S.

Funding: This research received no external funding.

Acknowledgments: The authors would like to thank Mats Hättestrand and Jan-Olof Nilsson for the continuous support during this work. Joakim Odqvist is acknowledged for his help with the Thermocalc calculations. Sandvik Materials Technology are acknowledged for providing the material and the hardness results.

Conflicts of Interest: The authors declare no conflict of interest. The funders had no role in the design of the study; in the collection, analyses, or interpretation of data; in the writing of the manuscript, or in the decision to publish the results.

References

1. Sha, W.; Guo, Z. *Maraging steels: Modelling of microstructure, properties and applications*; Woodhead Publishing Ltd.: Cambridge, UK, 2009; pp. 10–14.
2. Floreen, S. The physical metallurgy of maraging steels. *Metall. Rev.* **1968**, *13*, 115–128.
3. Millan, J.; Ponge, D.; Raabe, D.; Choi, P.; Dimitrieva, O. Characterization of nano-sized precipitates in a Mn-based lean maraging steel by atom probe tomography. *Steel Res.* **2011**, *82*, 137–145. [CrossRef]
4. Schnitzer, R.; Schober, M.; Zinner, S.; Leitner, H. Effect of Cu on the evolution of precipitation in an Fe-Cr-Ni-Al-Ti maraging steel. *Acta Mater.* **2010**, *58*, 3733–3741. [CrossRef]
5. Leitner, H.; Schober, M.; Schnitzer, R. Splitting phenomenon in the precipitation evolution in an Fe-Ni-Al-Ti-Cr stainless steel. *Acta Mater.* **2010**, *58*, 1261–1269. [CrossRef]
6. Ping, D.H.; Ohnuma, M.; Hirakawa, Y.; Kadoya, Y.; Hono, K. Microstructural evolution in 13Cr-8Ni-2.5Mo-2Al martensitic precipitation-hardened stainless steel. *Mater. Sci. Eng. A* **2005**, *394*, 285–295. [CrossRef]
7. Tian, J.; Wang, W.; Shahzad, M.B.; Yan, W.; Shan, Y.; Jian, Z.; Yang, K. A new maraging steel with excellent strength-toughness-corrosion synergy. *Materials* **2017**, *10*, 1293. [CrossRef] [PubMed]
8. Sun, L.; Simm, T.H.; Martin, T.L.; McAdam, S.; Galvin, D.R.; Perkins, K.M.; Bagot, P.A.J.; Moody, M.P.; Ooi, S.W.; Hill, P.; et al. A novel ultra-high strength maraging steel with balanced ductility and creep resistance achieved by nanoscale ß-NiAl and Laves phase precipitates. *Acta Mater.* **2018**, *149*, 285–301. [CrossRef]
9. Nilsson, J.-O.; Hultin Stigenberg, A.; Liu, P. Isothermal formation of quasicrystalline precipitates and their effect on strength in a 12Cr-9Ni-4Mo maraging stainless steel. *Metall. Trans. A* **1994**, *25*, 2225–2233. [CrossRef]
10. Liu, P.; Hultin Stigenberg, A.; Nilsson, J.-O. Quasicrystalline and crystalline precipitation during isothermal tempering in a 12Cr-9Ni-4Mo maraging stainless steel. *Acta Metall.* **1995**, *43*, 2881–2890. [CrossRef]
11. Hättestrand, M.; Nilsson, J.-O.; Stiller, K.; Liu, P.; Andersson, M. Precipitation hardening in a 12%Cr-9%Ni-4%Mo-2%Cu stainless steel. *Acta Mater.* **2004**, *52*, 1023–1037. [CrossRef]
12. Thuvander, M.; Andersson, M.; Stiller, K. Precipitation process of martensitic PH stainless steel Nanoflex. *Mater. Sci. Technol.* **2012**, *28*, 695–701. [CrossRef]

13. Stiller, K.; Hättestrand, M.; Danoix, F. Precipitation in 9Ni-12Cr-2Cu maraging steels. *Acta Mater.* **1998**, *46*, 6063–6073. [CrossRef]
14. Andersson, M.; Stiller, K.; Hättestrand, M. Comparison of early stages of precipitation in Mo-rich and Mo-poor maraging stainless steels. *Surf. Interf. Anal.* **2007**, *39*, 195–200. [CrossRef]
15. Stiller, K.; Andrén, H.-O.; Andersson, M. Precipitation in maraging and martensitic chromium steels - What can we learn using 3-DAP and EFTEM. *Mater. Sci. Technol.* **2008**, *24*, 633–640. [CrossRef]
16. Thuvander, M.; Andersson, M.; Stiller, K. Atom probe tomography investigation of lath boundary segregation and precipitation in a maraging stainless steel. *Ultramicroscopy* **2013**, *132*, 265–270. [CrossRef] [PubMed]
17. Kelly, T.F.; Larson, D.J. Local electrode atom probes. *Mater. Character.* **2000**, *44*, 59–85. [CrossRef]
18. De Geuser, F.; Lefebvre, W.; Blavette, D. 3D atom probe study of solute atoms clustering during natural ageing and pre-ageing of an Al-Mg-Si alloy. *Phil. Mag. Lett.* **2006**, *86*, 227–234. [CrossRef]
19. Hofer, F.; Warbichler, P.; Grogger, W. Imaging of nanometer-sized precipitates in solids by electron spectroscopic imaging. *Ultramicroscopy* **1995**, *59*, 15–31. [CrossRef]
20. Warbichler, P.; Hofer, F.; Hofer, P.; Letofsky, E. On the application of energy-filtering TEM in materials science: III. Precipitates in steel. *Micron* **1998**, *29*, 63–72. [CrossRef]